Aromatic Zipper Topology Dictates Water-Responsive Actuation in Phenylalanine-Based Crystals

Fahmeed K. Sheehan, Haozhen Wang, Darjan Podbevšek, Elma Naranjo, Janel Rivera-Cancel, Cooper Moran, Rein V. Ulijn, and Xi Chen**

Water-responsive (WR) materials that reversibly deform in response to relative humidity (RH) changes are gaining increasing interest for their potential in energy harvesting and soft robotics applications. Despite progress, there are significant gaps in the understanding of how supramolecular structure underpins the reconfiguration and performance of WR materials. Here, three crystals are compared based on the amino acid phenylalanine (F) that contain water channels and F packing domains that are either layered (F), continuously connected (phenylalanyl-phenylalanine, FF), or isolated (histidyl-tyrosyl-phenylalanine, HYF). Hydration-induced reconfiguration is analyzed through changes in hydrogen-bond interactions and aromatic zipper topology. F crystals show the greatest WR deformation (WR energy density of 19.8 MJ m^{-3}) followed by HYF (6.5 MJ m^{-3}), while FF exhibits no observable response. The difference in water-responsiveness strongly correlates to the deformability of aromatic regions, with FF crystals being too stiff to deform, whereas HYF is too soft to efficiently transfer water tension to external loads. These findings reveal aromatic topology design rules for WR crystals and provide insight into general mechanisms of high-performance WR actuation. Moreover, the best-performing crystal, F emerges as an efficient WR material for applications at scale and low cost.

1. Introduction

WR materials mechanically transform in response to changes in RH or water gradient, converting the chemical potential of water into mechanical actuation. Driven by the urgent need to develop alternative, greener energy technologies, there have recently been many innovations in the field of WR materials and in the use of these emerging materials for various applications, including RH sensing,[1–4] artificial muscles,[5–7] microscopic machines,[8,9] and new types of energy harvesting.[10–12] Despite promising advances in the context of stimuli-responsive materials,[13] there are still basic questions about how water movement at the molecular level translates to materials' macroscale deformation.

Short peptides are particularly attractive as a platform to address fundamental chemical and physical questions owing to their well-understood self-assembly behaviors and sequence-encoded properties.[14–17] The chemical complexity of their backbone and side-chain interactions grants peptides highly diverse structures and functionalities.[18–22] Self-assembling peptides designed using these principles have been demonstrated to form stimuli-responsive materials.[18,23] As an example, peptide-based systems have been reported to have dynamic pores, which can be reversibly opened or closed using different stimuli.[24–26]

Recently, we found that rationally selected tripeptide crystals composed of tyrosine-phenylalanine (YF) aromatic dyads, and in particular HYF, exhibit significant, reversible changes in their lattice structures upon RH changes.[14,27] These peptide-based WR crystals are an especially promising platform for the study of water-responsiveness, as their molecular level WR movements can be monitored directly using crystallographic methods. The tripeptide crystals of HYF, DYF, and YFD (D: aspartic acid. D-containing peptides were C-terminal amidated) all possess hierarchical architectures containing aqueous and aromatic regions that are connected through non-covalent networks, but only HYF crystals show high WR performance. HYF's significant water-responsiveness was attributed to the enhanced water binding in aqueous pores upon dehydration, and the presence of reconfigurable aromatic pockets interspersed with these pores, collectively leading to a tension that translated from its pores to deform the crystal structure.

F. K. Sheehan, H. Wang, D. Podbevšek, E. Naranjo, J. Rivera-Cancel, R. V. Ulijn, X. Chen
Advanced Science Research Center (ASRC) at the Graduate Center of the City University of New York
85 St. Nicholas Terrace, New York, NY 10031, USA
E-mail: rulijn@gc.cuny.edu; xchen@gc.cuny.edu

F. K. Sheehan, J. Rivera-Cancel, R. V. Ulijn, X. Chen
Ph.D. Program in Chemistry
The Graduate Center of the City University of New York
365 5th Ave, New York, NY 10016, USA

F. K. Sheehan, C. Moran, R. V. Ulijn
Department of Chemistry
Hunter College
695 Park Ave, New York, NY 10065, USA

H. Wang, X. Chen
Ph.D. Program in Physics
The Graduate Center of the City University of New York
365 5th Ave, New York, NY 10016, USA

E. Naranjo, X. Chen
Department of Chemical Engineering
The City College of New York
275 Convent Ave, New York, NY 10031, USA

The ORCID identification number(s) for the author(s) of this article can be found under https://doi.org/10.1002/smll.202207773.

DOI: 10.1002/smll.202207773

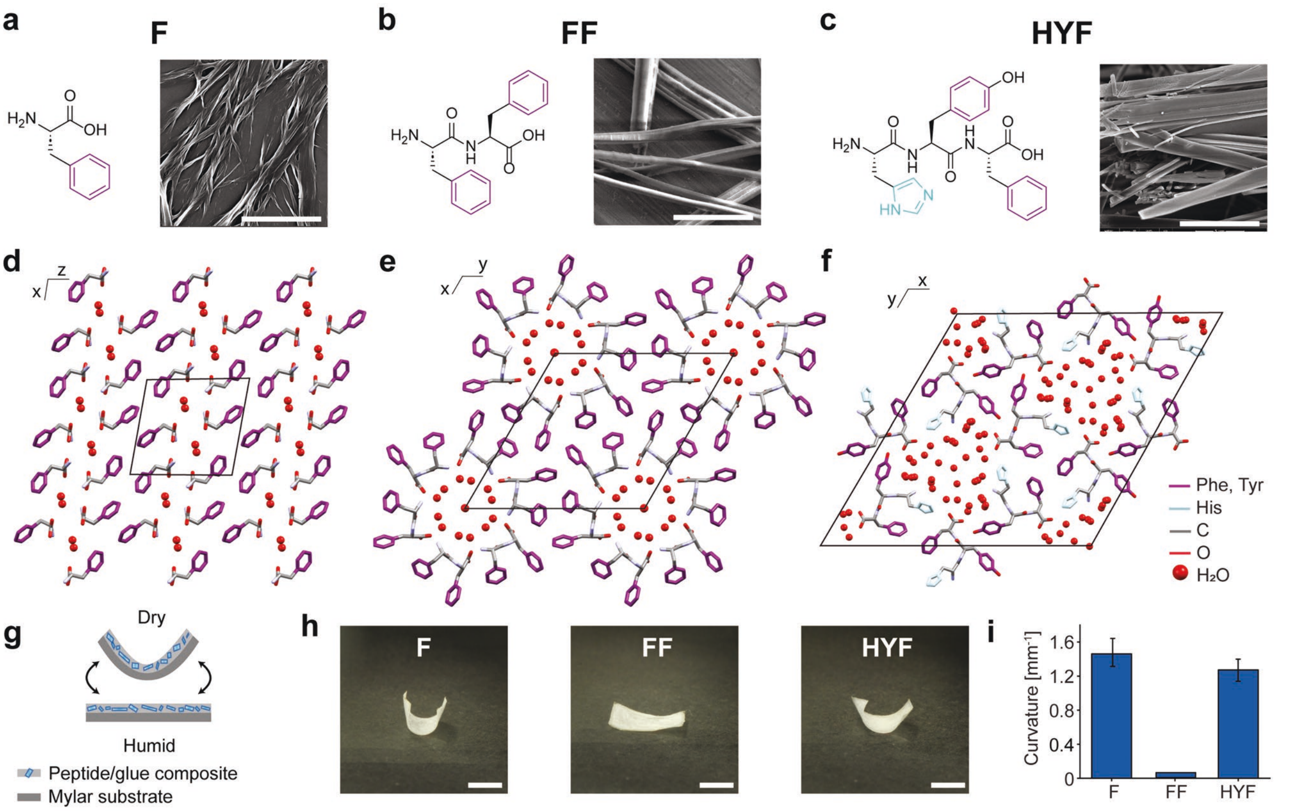

Figure 1. WR F-based crystals with different aromatic topologies. a–c) Molecular structures of F, FF, and HYF, followed by scanning electron microscope (SEM) images of the crystals they form. Scale bar 5 µm d–f) Hydrated crystal structures of F, FF, and HYF.[27,30,40] g) Schematic representation of the bilayer film curvature at different RH. h) The appearance of each crystal film at 10% RH. Scale bar 2 mm. i) The average maximum curvature from a sample set of three films (*n* = 3).

Despite the importance of the H-bonding network of aqueous channels in F-based crystals' water-responsiveness, it is uncertain what fundamental role the topology of the aromatic regions plays in tuning the WR behavior. We hypothesize that, even if the inter-pore chemistry and H-bonding network are amenable to WR actuation, the aromatic layers must be stiff, but sufficiently deformable to accommodate significant WR actuation. Crystals that are too tightly packed will be unable to deform, whereas too much deformability will make the crystal unstable and collapse at any water tension.

To elucidate the role of the topology of the aromatic motif in amino acid and peptide crystals in modulating the WR behavior, we selected crystals of F, FF, and HYF (**Figure 1**a–c), which contain aqueous channels and aromatic regions, but with very different aromatic stacking,[28] namely layered, continuously connected, and interspersed pockets (Figure 1d–f). Each of these molecules can self-assemble into high aspect-ratio crystals (Figure 1a–c; Figure S1,S2, Supporting Information). The crystal structures of F and FF have been widely studied:[28–42] it is known that F can form numerous different crystal polymorphs according to crystallization conditions, including a dynamic crystal phase change triggered by changing RH[40,41] which produces hydrated and dehydrated phases. FF is known to form extremely rigid nanotubes with large nanopores populated by structurally bound water at the pore interface surrounding mobile water.[30,31]

2. Results and Discussion

To assess if F, FF, and HYF crystals exhibit different WR behaviors at the macroscopic level, a bilayer film experiment was performed, whereby a layer of a crystal-glue composite on top of a Mylar film can cause the film to curve at low RH (Figure 1g). The adhesive glue mechanically couples the actuation of the crystals to the curling of the film. When responding to RH changes, the films with F and HYF crystals showed reversible curling actuation, with a maximum curvature of 1.44 mm^{-1} for F and 1.276 mm^{-1} for HYF (Figure 1h,i). To our surprise, the FF film showed essentially no response to RH changes, while F shows a stronger response compared to HYF. Notably, the bilayer films of F crystals can reversibly bend and straighten in response to RH changes at various temperatures (Figures S3–S5, Supporting Information), and they show no performance degradation after 1400 RH cycles (Figure S6, Supporting Information).

F, FF, and HYF crystals' microscale water-responsiveness and mechanical properties were assessed using an RH-controlled atomic force microscopy (AFM), which allows for adjustment of local RH near the sample. AFM topographies show distinct WR properties of F, FF, and HYF crystals as RH increased from 10% to 90% (**Figure 2**a,b). Based on the transverse height difference of the crystals at different RH levels, we calculated the WR strain of F to be 22%, which is higher than the previously

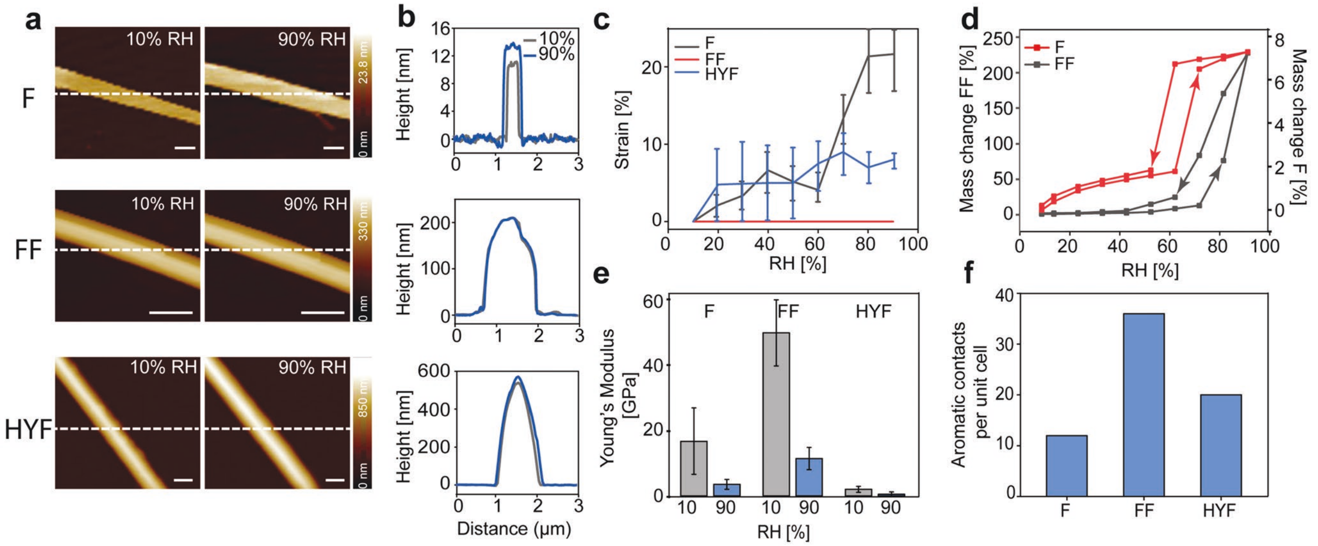

Figure 2. Microscale WR properties of F, FF, and HYF. a) AFM topographies of each F-based crystal, followed by b) a height trace at 10% and 90% RH. c) The WR strain calculated by comparing the heights of crystals at different RH to the height at 10% RH ($n = 3$). d) Water sorption isotherms of F and FF against RH. e) Young's Moduli of F, FF, and HYF crystals at 10% and 90% RH ($n = 3$). f) The number of strong aromatic interactions per unit cell in F, FF, and HYF.

reported WR strain for HYF of 8% (Figure 2c). However, FF crystals do not show any deformation in response to RH. The results are consistent with the crystal's macroscale WR behaviors observed in the bilayer film experiments (Figure 1h,i).

To further probe the water-uptake behaviors of the crystals, we performed dynamic vapor sorption (DVS) experiments. We found that, while FF crystals show no WR actuation, they adsorbed water up to 220% of their weight at 90% RH (Figure 2d). We note that this value differs from results reported by other groups,[34] which may be due to residual interfacial non-polar solvents used during the assembly process in previous reports. HYF also showed significant water adsorption up to 148%.[27] The high level of water adsorption of HYF and FF crystals is likely due to the high surface area formed during the aqueous self-assembly and evaporation-driven crystallization of these hierarchical porous materials.[44] By contrast, F showed a much lower level of adsorption of 7.4%. The three systems studied exhibit hysteresis, which for F and HYF coincides with their responsive RH intervals (60–70% for F, 20–30% for HYF). The sharp hysteresis isotherms observed for F and HYF indicate a stoichiometric hydrate effect, where the hydration of the crystal does not occur until the designated RH is reached. The FF hysteresis isotherm in contrast suggests a capillary condensation effect occurring in the mesopores between crystals. At the RH transition where F and HYF deform, water adsorption is more nominal: 6% for F and 18% for HYF. These observations suggest that there is no direct relation between water adsorption capability and WR actuation.

Nanoindentation experiments performed at low and high RH showed differences in stiffness among the crystals in dry and humid conditions (Figure S7, Supporting Information; Figure 2e, **Table 1**). At 10% RH, we recorded stiffnesses of 16.5, 49.2, and 2 GPa respectively, which reduced to 3.5, 11.3, and 0.5 GPa at 90% RH. Comparing F and FF, we attribute the difference in stiffness to the tightly packed aromatic zipper in FF as opposed to the weaker stacking interactions in F (Figure 2f). It is understood that the high rigidity of FF crystals can be largely attributed to dispersion interactions in its aromatic zipper,[45] with a more recent study noting the role of water in the FF channel in bestowing FF with unusually high rigidity.[46] The further reduction of stiffness in HYF compared to F is a result of the isolated aromatic pockets of HYF instead of the continuous or layered zippers in FF or F. The aromatic topology of HYF leads to a softer crystal than either F or FF. Using the measured Young's moduli and WR strain, we can estimate the WR energy density from the elastic energy difference between dry and wet crystals. (Table 1)

To gain further insight into the changes in crystal packing upon dehydration, we performed environmentally controlled powder X-ray diffraction (PXRD) on F and FF (**Figure 3**a,b) to compare to our previously reported data for HYF.[27] The crystal samples were confined in an enclosed chamber where RH could be manually regulated during the collection of diffraction patterns at regular RH intervals. Existing crystal analyses were used as references for our data.[38,41,47–49] A major phase change in F is observed as RH is raised from 60% to 70% (Figure 3a), corresponding to an expansion of the crystal at higher RH. By contrast, FF shows no change in diffraction pattern (Figure 3b), suggesting no phase transition occurs over the entire RH range

Table 1. Young's moduli at 10% and 90% RH and energy densities of F, FF, and HYF[27] crystals, along with the maximal water adsorption at 90% RH.

	Stiffness at 10% RH [GPa]	Stiffness at 90% RH [GPa]	Energy density [MJ m^{-3}]	Max water adsorption (% of total weight)
F	16.5	3.5	19.8	7.5
FF	49.2	11.3	–	220
HYF	2	0.5	6.5	148

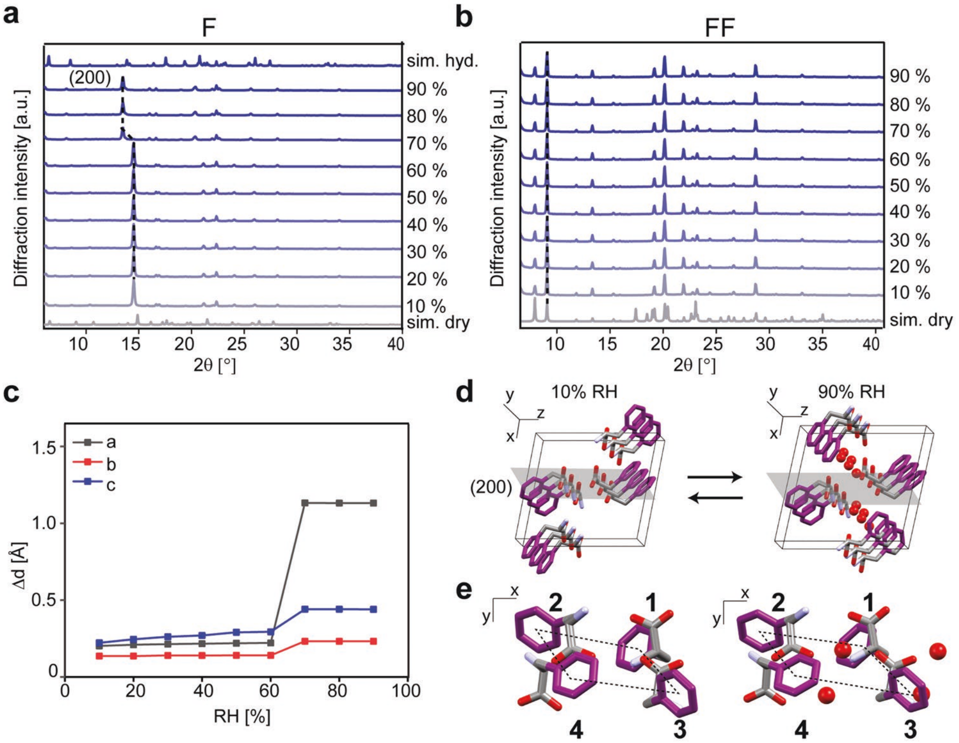

Figure 3. PXRD analysis on F crystals. a) PXRD patterns of F crystals with varying RH. Dashed line tracks the 200 plane. Sim. hyd. and sim. dry refer to diffraction patterns calculated from the corresponding crystal structure. b) PXRD patterns of FF crystals with varying RH. c) Refined lattice parameter shifts in F with varying RH. d,e) Representation of the two crystal phases of F at 10% and 90% RH.[41]

studied. Compared to the unit cell of the F crystal at 10%, the diffraction pattern at 90% RH indicates that the lattice parameters of a, b, and c increase by 7.6%, 1.0%, and 1.5%, respectively (Figure 3c), corresponding with the two known crystal phases of F (Figure 3d). The previously reported HYF crystal showed reduced lattice parameter changes of 2.8%, 2.8%, and 1.8%[27] compared to those of F. These results agree with the trend observed in macroscopic bilayer films and AFM experiments, with F changing in phase at the same RH values (Figures 1h and 2c). Despite more water adsorbed for FF crystals (Figure 2d), the bending of the bilayer films is a consequence of WR deformation of the crystals, and the reduced deformability of the FF crystal leads to a low bending curvature of its bilayer film. The higher WR strain (22%) of F crystals observed through AFM analysis can be rationalized by considering that F nanofibers are bundles of many crystals. We interpret these lattice parameter changes in terms of dehydration-induced stress that applies tension to the structural aromatic regions of the crystal. In F crystals, the stiff but deformable aromatic topology permits the phenyl moieties to shift in response to tension, resulting in a shrinkage of water channels while maintaining the crystal form (Figure 3d,e, **Table 2**). On the other hand, the softer HYF crystals cannot withstand the tension and maintain their crystal structures at low RH,[27] and the more stable aromatic region of FF crystals prevents any deformation during dehydration.

Fourier transform infrared spectroscopy (FTIR) analysis reveals further molecular-level interactions during their WR actuation (**Figure 4**). When RH decreases from 70% to 60%, the peaks at 1407 cm^{-1} (symmetric C—O stretching) and 1506 cm^{-1} (symmetric N—H bending) for F shifts to lower wavenumbers (Figure 4a; Figure S8, Supporting Information), indicating a dehydration-induced strengthening of backbone-backbone interactions, corresponding with the phase of F (Figure 3a). A

Table 2. Distances and relative orientations between adjacent phenyl rings.

F at 10% RH				F at 90% RH			
Centroid	Centroid*	Distance [Å]	Orientation [°]	Centroid	Centroid*	Distance [Å]	Orientation [°]
1	3	4.81	52.47	1	3	4.78	57.82
1	4	6.02	14.48	1	4	5.95	20.57
1	2	5.99	59.43	1	2	6.02	69.54
3	4	6.28	52.47	3	4	7.28	57.82
2	4	5.22	62.65	2	4	5.23	74.73

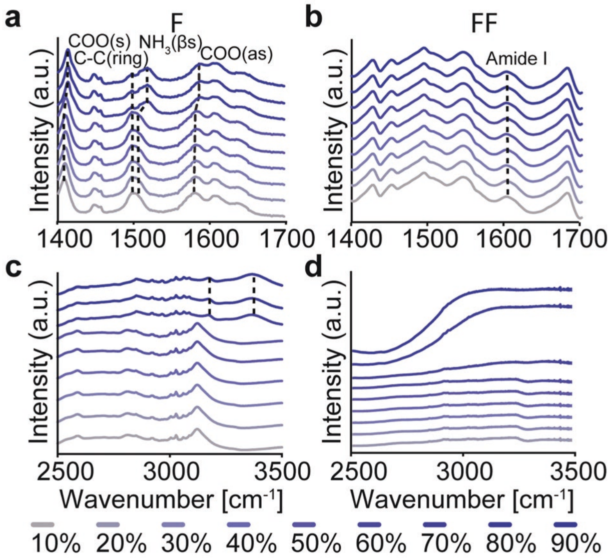

Figure 4. FTIR spectra of F and FF with varying RH a) and b) between 1400 and 1700 cm^{-1} and c) and d) between 2500 and 3500 cm^{-1}.

similar phenomenon is observed in the FTIR spectra for HYF crystals.[27] In the FF spectrum, we observe the amide I peak at 1602 cm^{-1}, with a shoulder at 1620 cm^{-1} confirming its β-sheet character[50] (Figure 4b). The FF spectra do not change with shifting RH.

A number of prominent changes occur in the 2500–3500 cm^{-1} region (Figure 4c), including the emergence of a dominant peak at 3371 cm^{-1} and a smaller peak at 3174 cm^{-1} (highlighted in Figure 4c). These peaks may hint toward the presence of two different populations of water. The presence of these peaks only after the crystal phase change RH of 60–70% confirms that the peak shifts observed are not adsorption-induced.[51] Water peaks in the spectra for FF are also observed ≈3250 cm^{-1} (Figure 4d), but at higher RH values adsorbed water saturates the detector, agreeing with the high level of water adsorption for FF observed in DVS experiments (Figure 2d). Both sets of spectra agree with the data obtained from PXRD and DVS.

HYF has been previously demonstrated to undergo a reversible structure collapse between 20–30% RH.[27] The specific molecular architecture of HYF causes a strengthening in intermolecular H-bonding along the lining of the pore upon dehydration, dramatically shrinking the pore and inducing a loss in crystallinity. Crucially, the aromatic pockets confer sufficient rigidity to prevent a complete, irreversible loss in structure, yet remain flexible enough to deform around the aqueous pore. Breaching the 30% RH threshold introduces enough water to restore the pore structure and, consequently, the crystalline arrangement, which remains unchanged at higher RH levels.

The WR reconfiguration of F crystals follows a different path, enabled by the layered arrangement of charge-complementary backbone stacks, with parallel, linear hydrophobic aromatic zipper domains.[38] The aromatic zipper motif of F grants F higher stiffness than the aromatic pockets in HYF. Consecutive aromatic rings in F interact weakly with each other, allowing them to slide past each other to accommodate water molecules in between the ion-complementary channel in a distinct manner to the deformation observed in HYF (Figure 3a). In the case of F, interacting backbone carboxyl and amine groups readily separate to bind to water molecules at RH values exceeding 60%. Along with the aromatic zipper, the ionic backbone channel influences overall crystal stability and orientation.[52] Therefore, the aromatic stacking in F confers enough stability to prevent complete crystal collapse at low RH (which we observe in HYF) but are not so stiff as to prevent such a translation (as in FF). We also speculate that the different critical RH thresholds for F and HYF relate to both the H-bonding strength of aqueous channels and aromatic deformability.

3. Conclusion

In conclusion, upon comparing F, FF, and HYF crystals, only F and HYF show WR behavior with different phase transition RH and energy densities, while FF was found to be unresponsive. We found that the WR activity of the crystals can be related to the deformability of the aromatic topologies supporting each crystal, dictating whether a crystal transition can be accommodated with retention of overall structure integrity. We propose that there is an optimum range of deformability between which water-responsiveness is possible – beyond this range, the crystals either lose crystallinity, or are too rigid to accommodate structural transformations. We also found that water adsorption capacity varies greatly (7.6%, 220%, and 148% for F, FF, and HYF respectively) among these three systems, and that it is not correlated to the responsiveness of crystals. We therefore provide new insights in design criteria for WR materials, highlighting the structural topology of the crystal as a means of tuning WR-behavior in addition to the water-binding ability of the aqueous pores. Further, F-based crystals, especially F crystals, have emerged as promising materials for designing large-scale WR systems owing to their sequence-tunable WR properties through aromatic topology, high energy density, (F crystals' WR energy density is nearly three orders of magnitude greater than that of human muscle[53]), low cost ($30 per kg for F) and their FDA GRAS (generally regarded as safe) status. In ongoing work, we are exploring the use of WR peptide and amino acid crystals to design embedded devices in or on the body for RH-driven artificial muscles, as components in energy harvesting machines, and in biosensing applications.

4. Experimental Section

Materials: Amino acid (AA) F (98%) and dipeptide FF (98%) peptides were obtained from Sigma–Aldrich and were used as purchased. HYF (95%) was obtained from CSBio and used after TFA removal via three HCl (10 mM) washes. HYF was dissolved directly into HCl (0.1 M) solution to the final concentration of peptide (1 mg mL^{-1}). The solution was then lyophilized, and the process was repeated for subsequent washes. The TFA content was found to be <1% after the sample was quantified via ^{19}F NMR (Avance III HD 300, Bruker). The deionized water was filtered in lab (MilliQ, Millipore). All other solvents were purchased from Sigma–Aldrich.

Crystal Preparation: Each species was added to the requisite concentration (150 mM for F, 5 mM for FF, 5 mM for HYF) in DI water, heated to 70 °C on a heat-block shaker (Echotherm, Torrey Pines

Scientific) for 5 min to dissolve, and left to cool at room temperature for 24 h. Crystals form spontaneously upon cooling for FF and HYF. F crystals form upon drying.

Macro-Scale Bilayer Films Preparation: To prepare the macro-scale crystal bilayer films, crystal-glue composites were deposited on 5 mm × 3 mm × 6 µm Mylar films. Before deposition, Mylar films were treated by plasma (M1070 NanoClean, Fischione) at 100% power, 75% argon and 25% oxygen for 30 s. Aqueous crystal suspensions at different concentrations (150 mmol kg^{-1} for F, 20 mmol kg^{-1} for FF, 5 mmol kg^{-1} for HYF) were mixed with a dilute Elmer's glue solution (Elmer's Products) at a 3:5 volume ratio before the mixture was pipetted onto films. The volume of composites to be pipetted was adjusted to form 16 µm thick composite layers after drying on a hot plate at 50 °C. The curvature of the films at 10% and 90% RH was recorded with a camera (Canon EOS Rebel SL1) and analyzed using ImageJ.

Crystal characterization: *WR Strain and Stiffness*: F, FF, and HYF crystal suspensions were deposited and air dried on a silicon wafer. The topography of the crystals was probed under various RH conditions using a customized AFM (Multimode 8, Bruker). The local RH near the samples was regulated by enclosing the AFM stage into a chamber with a RH sensor (HIH-4021-003, Honeywell) and applying a continuous flow of dry or humid air until desired RH levels reached equilibrium. RH environments were maintained for at least 5 minfor each RH level before measurements. Topographies were measured using an AFM probe with a tip radius of 2 nm (SCANASYST-AIR, Bruker) and characterized using Nanoscope Analysis (Bruker). The WR strain was calculated by normalizing the crystals' heights at various RH to the heights at 10% RH. For stiffness measurements, AFM nanoindentation was performed onto the crystal using a different probe (NCHV, Bruker) with tip radius 16 nm and spring constant 42 N m^{-1}. The shape of the curve produced by plotting force against indentation was used to calculate Young's Modulus following the Hertz model (Figure S7, Supporting Information):

$$F = \frac{4}{3}\frac{E}{1-\nu^2}R_{\text{tip}}^{\frac{1}{2}}h^{\frac{3}{2}} \tag{1}$$

where F is the force applied, E is the Young's Modulus of the crystal, ν is Poisson's ratio (estimated to be 0.3), R_{tip} is the radius of the tip, and h is the nanoindentation depth. A maximum force of 300 nN was used with a spherical AFM tip (NCHV, Bruker) with tip radius 14 nm. The RH was stabilized at each interval before measurements were taken. The energy density of the crystals was estimated from the elastic energy difference between crystals at 10% and 90% RH:

$$U_{\text{m}} = \frac{1}{4}(E_{10} - E_{90})\varepsilon^2 \tag{2}$$

where U_{m} is the energy density, E_{10} and E_{90} are the Young's moduli of the crystal at 10% and 90% RH respectively, and ε is the WR strain across the crystal between 10% and 90% RH.

Water Sorption Isotherms: Water sorption isotherms of F, FF, and HYF crystals were measured by a DVS equipment (DVS Intrinsic, Surface Measurement Systems) with dried crystals (5 mg) loaded. The RH was alternated between 10% and 90% at 25 °C, and the mass change of the crystals was measured in real-time. To ensure environmental equilibrium, RH was shifted to the next level when the mass change rate (dm dt^{-1}) was maintained at 0.01 mg min^{-1} for 5 min, or the RH level was maintained for 20 min. The water sorption isotherms were calculated by the DVS control software and averaged from three tests with replicated hydration/dehydration cycles.

Crystal Phase Transitions: The structures of F, FF, and HYF crystals were confirmed by PXRD. Crystals were deposited on glass slides and their X-ray diffraction was measured directly in a powder X-ray Diffractometer (X'Pert Pro, Malvern Panalytical). The X-ray source was a Philips high intensity ceramic sealed Cu tube at 3 kW, wavelength 1.5405 Å. The diffracted beam passed through a Ni filter before reaching a $\text{PIXcel}^{\text{1D}}$ detector. The local RH near the samples was regulated by enclosing the sample holder in a custom acrylic tube with thin, radiolucent Mylar windows to allow X-rays to travel unobstructed. RH was regulated by controlling the ratio of dry and humid air injected through a thin tube facing the sample. RH values were monitored by using an RH sensor (HIH-4021-003, Honeywell) placed near the sample and allowed to equilibrate at least 10 min between measurements. Diffraction patterns were collected in 10% RH intervals for two hydration/dehydration cycles. Patterns were compared against simulated diffraction patterns based on the crystal structures submitted in.[41] Lattice parameters for F were calculated by pattern fitting and performing Pawley refinement (GSAS II) against parameters drawn from the known structures of hydrated and dehydrated F.[43]

FTIR: Crystals were deposited between CaF_2 windows separated by a 27 µm polytetrafluoroethylene spacers mounted into a flow cell. Spectra were collected with 2 cm^{-1} resolution in an FTIR spectrometer (Vertex 70, JASCO). RH was regulated with a RH sensor (HIH-4021-003, Honeywell) placed in a separate enclosed chamber, with an inlet for dry/humid air and an outlet that led directly to the flow cell. RH values were allowed to equilibrate at least 10 min between measurements. Spectra were collected for two hydration/dehydration cycles with 10% RH intervals.

Statistical Analysis: For statistical analyses, there was no pre-processing of data. All experimental data are presented as mean ± SD with $n = 5$, unless otherwise noted. Statistical analysis was carried out using Python.

Supporting Information

Supporting Information is available from the Wiley Online Library or from the author.

Acknowledgements

The authors thank the Army Research Office for supporting this work, award no. W911NF-21-1-0172.

Conflict of Interest

The authors declare no conflict of interest.

Data Availability Statement

The data that support the findings of this study are available from the corresponding author upon reasonable request.

Keywords

aromatic zippers, peptide crystals, stiffness, water-responsive materials

Received: December 12, 2022
Revised: February 28, 2023
Published online:

[1] S. Kano, K. Kim, M. Fujii, *ACS Sens* **2017**, *2*, 828.
[2] D. Zhang, J. Tong, B. Xia, Q. Xue, *Sens. Actuators B.* **2014**, *203*, 263.
[3] U. Mogera, A. A. Sagade, S. J. George, G. U. Kulkarni, *Sci. Rep.* **2014**, *4*, 4103.
[4] P. Li, N. Su, Z. Wang, J. Qiu, *ACS Nano* **2021**, *15*, 16811.
[5] H. Wang, Z.-L. Liu, J. Lao, S. Zhang, R. Abzalimov, T. Wang, X. Chen, *Adv. Sci.* **2022**, *9*, 2104697.

[6] Y. Park, Y. Jung, T.-D. Li, J. Lao, R. S. Tu, X. Chen, Y. Park, Y. Jung, T. Li, R. S. Tu, X. Chen, J. Lao, X. C. Program, *Macromol. Rapid Commun.* **2020**, *41*, 1900612.

[7] I. Agnarsson, A. Dhinojwala, V. Sahni, T. A. Blackledge, *J Exp Biol* **2009**, *212*, 1990.

[8] B. Shin, J. Ha, M. Lee, K. Park, G. Ho Park, T. Hyun Choi, K.-J. Cho, H.-Y. Kim, *Sci Robot* **2018**, *3*, 2629.

[9] Y. Q. Liu, Z. di Chen, D. D. Han, J. W. Mao, J. N. Ma, Y. L. Zhang, H. B. Sun, *Adv. Sci.* **2021**, *8*, 2002464.

[10] X. Chen, D. Goodnight, Z. Gao, A. H. Cavusoglu, N. Sabharwal, M. Delay, A. Driks, O. Sahin, *Nat. Commun.* **2015**, *6*, 7346.

[11] M. Yang, S.-Q. Wang, Z. Liu, Y. Chen, M. J. Zaworotko, P. Cheng, J.-G. Ma, Z. Zhang, *J Am Chem Soc* **2021**, *143*, 7732.

[12] M. Ma, L. Guo, D. G. Anderson, R. Langer, *Science* **2013**, *339*, 186.

[13] S. Y. Park, X. Chen, Y. Park, P. X. Chen, *J. Mater. Chem. A* **2020**, *8*, 15227.

[14] P. W. J. M. Frederix, G. G. Scott, Y. M. Abul-Haija, D. Kalafatovic, C. G. Pappas, N. Javid, N. T. Hunt, R. V. Ulijn, T. Tuttle, *Nat. Chem.* **2015**, *7*, 30.

[15] A. Lampel, S. A. McPhee, H. A. Park, G. G. Scott, S. Humagain, D. R. Hekstra, B. Yoo, P. W. J. M. Frederix, T. de Li, R. R. Abzalimov, S. G. Greenbaum, T. Tuttle, C. Hu, C. J. Bettinger, R. V. Ulijn, *Science* **2017**, *356*, 1064.

[16] A. Levin, T. A. Hakala, L. Schnaider, G. J. L. Bernardes, E. Gazit, T. P. J. Knowles, *Nat. Rev. Chem.* **2020**, *4*, 615.

[17] A. Dehsorkhi, V. Castelletto, I. W. Hamley, *J. Pept. Sci.* **2014**, *20*, 453.

[18] R. J. Mart, R. D. Osborne, M. M. Stevens, R. V. Ulijn, *Soft Matter* **2006**, *2*, 822.

[19] D. W. P. M. Lowik, E. H. P. Leunissen, M. van den Heuvel, M. B. Hansen, J. C. M. V. Hest, *Chem. Soc. Rev.* **2010**, *39*, 3394.

[20] I. W. Hamley, *Chem. Rev.* **2017**, *117*, 14015.

[21] N. J. Sinha, M. G. Langenstein, D. J. Pochan, C. J. Kloxin, J. G. Saven, *Chem. Rev.* **2021**, *121*, 13915.

[22] F. Sheehan, D. Sementa, A. Jain, M. Kumar, M. Tayarani-Najjaran, D. Kroiss, R. V. Ulijn, *Chem. Rev.* **2021**, *121*, 13869.

[23] A. Shah, M. S. Malik, G. S. Khan, E. Nosheen, F. J. Iftikhar, F. A. Khan, S. S. Shukla, M. S. Akhter, H. B. Kraatz, T. M. Aminabhavi, *Chem. Eng. J.* **2018**, *353*, 559.

[24] L. Zhang, J. B. Bailey, R. H. Subramanian, F. A. Tezcan, *Nature* **2018**, *557*, 86.

[25] C. Martí-Gastaldo, D. Antypov, J. E. Warren, M. E. Briggs, P. A. Chater, P. V. Wiper, G. J. Miller, Y. Z. Khimyak, G. R. Darling, N. G. Berry, M. J. Rosseinsky, *Nat. Chem.* **2014**, *6*, 343.

[26] D. F. Brightwell, G. Truccolo, K. Samanta, E. J. Fenn, S. J. Holder, H. J. Shepherd, C. S. Hawes, A. Palma, *Chemistry* **2022**, *28*, e202202368.

[27] R. Piotrowska, T. Hesketh, H. Wang, A. R. G. Martin, D. Bowering, C. Zhang, C. T. Hu, S. A. McPhee, T. Wang, Y. Park, P. Singla, T. McGlone, A. Florence, T. Tuttle, R. V. Ulijn, X. Chen, *Nat. Mater.* **2021**, *20*, 403.

[28] H. W. German, S. Uyaver, U. H. E. Hansmann, *J Phys Chem A* **2015**, *119*, 1609.

[29] T. O. Mason, D. Y. Chirgadze, A. Levin, L. Adler-Abramovich, E. Gazit, T. P. J. Knowles, A. K. Buell, *ACS Nano* **2014**, *8*, 1243.

[30] C. H. Görbitz, *Chem. Commun.* **2006**, *22*, 2332.

[31] M. Reches, E. Gazit, *Science* **2003**, *300*, 625.

[32] T. Das, M. Häring, D. Haldar, D. D. Díaz, *Biomater. Sci.* **2017**, *6*, 38.

[33] L. Adler-Abramovich, E. Gazit, *Chem. Soc. Rev.* **2014**, *43*, 6881.

[34] P. S. Zelenovskiy, E. M. Domingues, V. Slabov, S. Kopyl, V. L. Ugolkov, F. M. L. Figueiredo, A. L. Kholkin, *ACS Appl. Mater. Interfaces* **2020**, *12*, 27485.

[35] U. S. Raghavender, B. Chatterjee, I. Saha, A. Rajagopal, N. Shamala, P. Balaram, *J. Phys. Chem. B* **2011**, *115*, 9236.

[36] S. Bera, B. Xue, P. Rehak, G. Jacoby, W. Ji, L. J. W. Shimon, R. Beck, P. Král, Y. Cao, E. Gazit, *ACS Nano* **2020**, *14*, 1694.

[37] A. Datta, D. Bhattacharyya, S. Singh, A. Ghosh, A. Schmidtchen, M. Malmsten, A. Bhunia, *J. Biol. Chem.* **2016**, *291*, 13301.

[38] K. P. Nartowski, S. M. Ramalhete, P. C. Martin, J. S. Foster, M. Heinrich, M. D. Eddleston, H. R. Green, G. M. Day, Y. Z. Khimyak, G. O. Lloyd, *Cryst. Growth Des.* **2017**, *17*, 4100.

[39] D. Zaguri, S. Shaham-Niv, P. Chakraborty, Z. Arnon, P. Makam, S. Bera, S. Rencus-Lazar, P. R. Stoddart, E. Gazit, N. P. Reynolds, *ACS Appl. Mater. Interfaces* **2020**, *12*, 21992.

[40] H. M. Cuppen, M. M. H. Smets, A. M. Krieger, J. A. van den Ende, H. Meekes, E. R. H. van Eck, C. H. Görbitz, *Cryst. Growth Des.* **2019**, *19*, 1709.

[41] P. A. Williams, C. E. Hughes, A. B. M. Buanz, S. Gaisford, K. D. M. Harris, *J. Phys. Chem. C* **2013**, *117*, 12136.

[42] C. H. Gőrbitz, *Chemistry* **2001**, *7*, 5153.

[43] B. H. Toby, R. B. von Dreele, *J. Appl. Crystallogr.* **2013**, *46*, 544.

[44] C. Yuan, W. Ji, J. Li, E. Gazit, X. Yan, *Nat. Rev. Chem.* **2019**, *3*, 567.

[45] I. Azuri, L. Adler-Abramovich, E. Gazit, O. Hod, L. Kronik, *J. Am. Chem. Soc.* **2014**, *136*, 963.

[46] P. Zelenovskiy, I. Kornev, S. Vasilev, A. Kholkina, *Phys. Chem. Chem. Phys.* **2016**, *18*, 29681.

[47] B. Hernández, F. Pflüger, A. Adenier, S. G. Kruglik, M. Ghomi, *J. Phys. Chem. B* **2010**, *114*, 15319.

[48] R. Huang, R. Su, W. Qi, J. Zhao, Z. He, *Nanotechnology* **2011**, *22*, 245609.

[49] S. Olsztynska, M. K. Ska, L. Vrielynck, N. Dupuy, *Appl. Spectrosc.* **2001**, *55*, 901.

[50] X. Yan, Y. Cui, Q. He, K. Wang, J. Li, *Chem. Mater.* **2008**, *20*, 1522.

[51] S. Kudo, H. Ogawa, E. Yamakita, S. Watanabe, T. Suzuki, S. Nakashima, *Appl. Spectrosc.* **2017**, *71*, 1621.

[52] T. A. Watts, S. M. Niederberger, J. A. Swift, *Cryst. Growth Des.* **2021**, *21*, 5206.

[53] S. M. Mirvakili, I. W. Hunter, *Adv. Mater.* **2018**, *30*, 1704407.